JOURNAL OF MATERIALS SCIENCE 33 (1998) 3511–3517

Molecular organization in structural PVDF

D. GLENNON, P. A. COX, R. T. NEVELL, T. G. NEVELL, J. R. SMITH, J. TSIBOUKLIS*
School of Pharmacy and Biomedical Sciences, University of Portsmouth, St Michael's Building, White Swan Road, Portsmouth PO1 2DT, UK
E-mail: John.Tsibouklis@port.ac.uk

R. J. EWEN
Faculty of Applied Sciences, University of the West of England, Frenchay Campus, Coldharbour Lane, Bristol BS16 1QY, UK

Poly(vinylidene fluoride) containing 10% dibutyl sebacate plasticizer, as used in the construction of flexible oil and gas pipelines, has been exposed to raised temperatures for prolonged periods of time, to acid etching and to various tensile deformation regimes. The effects of these treatments on the crystallinity and surface properties of this material have been examined in the light of analytical data obtained by Fourier transform–infrared spectroscopy, differential scanning calorimetry, X-ray diffraction, X-ray photoelectron spectroscopy, goniometry and a variety of microscopy techniques. The results have shown that the molecular organization of this material can be influenced by the adoption of appropriate preconditioning procedures.

1. Introduction

Plasticizers, such as phthalates [1] and fatty acid esters [2], are often used to modify the bulk properties of poly(vinylidene fluoride) (PVDF), for engineering applications [3–6]. However, the physical and mechanical properties of polymeric materials are greatly influenced by the nature of their surfaces, and optical (OM) [7], transmission electron (TEM) [8] and scanning electron (SEM) [9] microscopies have been utilized for the study of PVDF surfaces. Such investigations are restricted by the resolution characteristics imposed by either the limitations of a particular technique or the inherent properties of the material, so that microscopic studies have tended to concentrate on the study of the larger-scale surface structures (e.g. spherulites, pore-size distributions). Atomic force microscopy (AFM) and scanning tunnelling microscopy (STM) have also been used to study larger scale surface features of PVDF [10–12]. In principle, however, these techniques may be capable of imaging surfaces with atomic resolution [13, 14].

Etching provides a readily accessible means of preparing highly crystalline polymer surfaces and this technique is used routinely in preparing such surfaces for high-resolution microscopy [15]. Several etching procedures are available, ranging from preferential dissolution of one component of a mixture [16], to permanganic oxidation [17]. Etching with fuming nitric acid selectively destroys the amorphous chain segments of polymer single crystals [18, 19], but no studies of the effect of this procedure on the surface chemistry of PVDF have, as yet, appeared in the literature. In this work, we report on our experiments to investigate the effects of various treatments on the molecular organization of plasticized PVDF. A range of well-established surface-characterization techniques (XPS, FT–IR, goniometry, TEM, OM) has been utilized to complement imaging by AFM, and the work is further supported by high-level molecular modelling calculations.

2. Experimental procedure

2.1. Materials, etching and stress procedures

A sample of PVDF (melting range 157–220 °C; containing 10 wt % dibutyl sebacate plasticizer) was taken directly from the inner sheath of an unused commercial flexible oil pipe. The sheath was cut longitudinally into curved strips which were machined into British Standard (BS 2782) [20] flat tensile testpieces ($l = 60 \pm 0.5$ mm, $w = 10 \pm 0.5$ mm, $t = 3 \pm 0.06$ mm). After conditioning (application of tensile stress and/or annealing, as appropriate), small film sections were produced as required by microtoming from the relevant area of the test-piece (centre of sample, or necked/failed region after stressing). The test-pieces were grouped according to the maximum tensile extension regime which they experienced: (1) unstrained, (2) elastic region, (3) onset of yield, (4) neck development, (5) neck stabilization, (6) mid-neck region, (7) end of neck region, and (8) failure. Each group was subjected

* Author to whom correspondence should be addressed.

to predetermined annealing conditions (unannealed, 100 and 130 °C) over predetermined time intervals ($a = 0$ h, $b = 3$ h, $c = 24$ h, $d = 1$ week, $e = 1$ month).

All samples were stressed to extend at a rate of 10 mm min^{-1}. After the appropriate conditioning, small film sections of the polymer were prepared from each specimen by microtoming along the loading axis from the relevant regions of the test-pieces and were examined by XRD and FT–IR spectroscopy. Selected film specimens (including etched samples) were then imaged by TEM and AFM. Prior to etching, two PVDF samples (1 cm × 1 cm) were melted and manually compressed between a glass slide and cover slip on a hot plate. One of the samples was etched with fuming nitric acid (80 °C, 10 min) then neutralized with 30% aqueous sodium hydroxide (0 °C) and rinsed with distilled water. The untreated sample was used as a control. Surfaces were examined by X-ray photoelectron spectroscopy (XPS) and contact angle goniometry.

2.2. Instrumentation

Tensile measurements were obtained using a Lloyd SR 100 instrument fitted with a 30 kN load cell. The internal extensometer was used to calibrate force–extension data. A Philips PW 1877 automated powder diffraction apparatus was used for XRD studies over the 2θ range 0°–80°. A cobalt tube anode was used, $K_{\alpha 1} = 0.7890$ nm and $K_{\alpha 2} = 0.7928$ nm (average = 0.7909 nm). FT–IR spectra were recorded using a Mattson RS/1 research series FT–IR instrument fitted with a beam condenser. All spectra were averaged over 100 scans at a resolution of 4 cm^{-1} over the range 4000–500 cm^{-1}. X-ray photoelectron spectroscopy (XPS) was carried out using a VG Scientific ESCALAB Mk.II employing a non-monochromatized Al–K_α source (1486.6 eV) operating at a power of 250 W. The analyser was operated at a constant pass energy of 10 eV. Lineshape analysis was performed on each peak and atomic percentages were calculated from the peak areas using standard atomic sensitivity factors [21]. AFM studies were performed in air under ambient conditions, using a Discoverer TopoMetrix TMX2000 scanning probe microscope (SPM) which was mounted on a custom-built mass/spring antivibration rig with a lateral natural frequency of 0.40 Hz and a vertical natural frequency of 0.52 Hz. Transmission electron microscopy (TEM) studies were performed using a Philips EM300 electron microscope.

2.3. Atomic force microscopy (AFM)

Scanners capable of maximum X–Y translations of (70 μm × 70 μm) and (1 μm × 1 μm) were used for studies of extrudate films and (0 0 1) surfaces, respectively. Imaging was performed in contact mode using standard-profile silicon nitride tips mounted on cantilevers of force constant 0.036 N m^{-1} for both the extrudates and etched samples. The rougher fold surfaces were scanned with a Supertip®, (Supertip® is a registered trademark of the TopoMetrix Corporation, Santa Clara, CA, USA.) Graphical output was displayed on a monitor with a resolution of 500 lines × 500 pixels. Images were levelled by plane-fitting and the atomic resolution image was filtered by two-dimensional fast Fourier transform (2D FFT).

2.4. Goniometry

Contact angles were measured using a Kernco contact angle goniometer fitted with an enclosed thermo-statted cell. Doubly distilled water (surface tension $\gamma_L = 73.4$ mN m^{-1} at 18.75 °C, literature value = 73.05 mN m^{-1} at 18 °C), diiodomethane (Aldrich Chemical Co. Ltd, >99%; $\gamma_L = 48.7$ mN m^{-1} at 18.8 °C, literature value = 50.76 mN m^{-1} at 20 °C) and 1,1-ethane diol (ethylene glycol, Aldrich Chemical Co. Ltd, > 99%; $\gamma_L = 47.7$ mN m^{-1} at 18.8 °C, literature value = 48.40 mN m^{-1} at 20 °C) were used as-supplied. Contact-angle measurements of droplets (2–3 μl) were recorded at 24 ± 1 °C using water, diiodomethane and 1,2-ethane diol.

3. Results and discussion

3.1. Effects of annealing

Unetched samples of PVDF were annealed at 130 °C for periods up to 7 days and subsequently stretched to onset of yield (group 3). The bulk crystallinity of annealed and/or stretched samples was then studied by XRD, and microtomed films were examined by FT–IR spectroscopy.

The dependence of load at yield, F_y, on annealing time, t, scaled as $x = t/80$ h is shown in Fig. 1. The superimposed function

$$F_y = 1108[1 - \exp(-37.59(x + 0.450)^4)] \quad (1)$$

fits closely with the experimental data. This reflects the analogy with the Avrami equation [20] for the kinetics of crystallisation

$$\varphi = \varphi_\infty[1 - \exp(-zt^n)] \quad (2)$$

where φ and φ_∞ are the volume fraction of crystalline material at time t and after an infinite length of time, respectively, z is the Avrami exponent and n is the

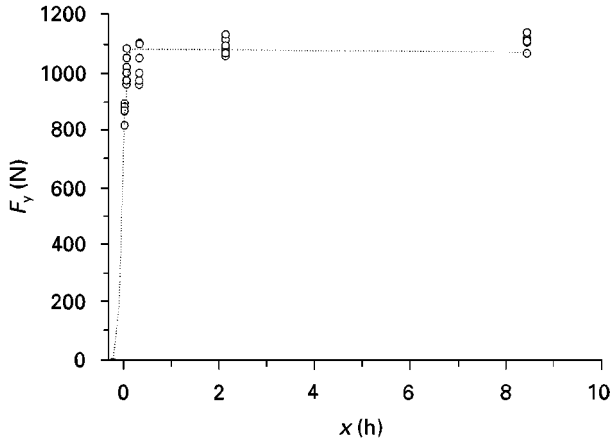

Figure 1 The effect of annealing time (130 °C) on the yield point, F_y of unetched PVDF. For the annealing period, six samples have been used to determine tensile extension points 3–8. (. . .) $F_y = 1108[1 - \exp(-37.59(x + 0.450)^4)]$.

Avrami index. Values $n = 2$ or 3 gave a less satisfactory fit (higher χ^2) but the scatter of data is such that no distinction can be made between values $n > 4$. An index of $n = 4$ is indicative of a heterogeneous nucleation process [22]. In this case, because annealing brings about secondary crystallization, and this was observed as a progressive increase in opacity, the fourth power is attributed to nucleation at pre-existing crystallites. The increase in maximum load on annealing can be explained in terms of secondary crystallization, hence

$$F_{max} = F_{max,\,\infty}[1 - \exp(-z'(t + \alpha)^{n'})] \qquad (3)$$

where F_{max} and $F_{max,\,\infty}$ are the maximum load at time t and $t = \infty$, respectively; z' and n' are the Avrami parameters. Because the Avrami equation represents crystallization from a completely amorphous phase, the constant α represents an empirical time correction to allow for partial crystallinity in unannealed samples. A detailed analysis of the mechanical testing experiments is to be found elsewhere [23].

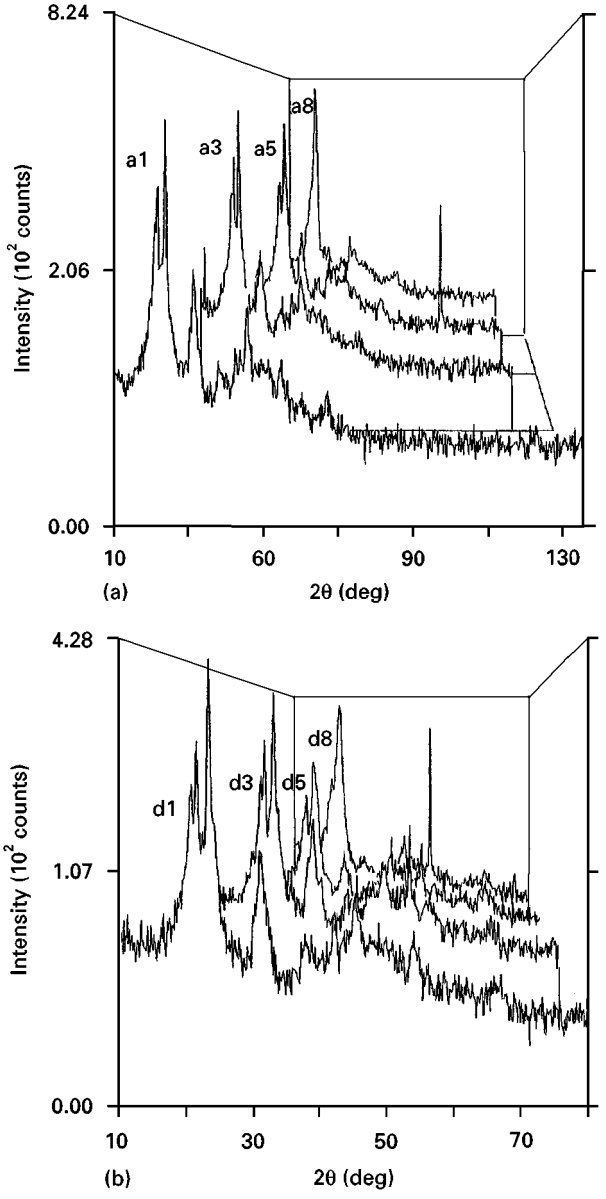

Figure 2 XRD intensity versus 2θ plots of (a) unannealed samples, and (b) samples annealed at 130 °C for 1 wk. Codes refer to groups of samples stressed to various stages (experimental).

From XRD, unannealed samples (Fig. 2a, in which diffraction patterns for groups 2, 4, 7 and 8 have been omitted for clarity) contain the three main phases of PVDF (α, β and γ) [24]. The proportion of the α-phase present decreases with increasing tensile deformation as evinced by decreasing intensities of the (1 1 0) reflection ($2\theta = 12^\circ$, $d_{hkl} = 0.490$ nm) and the (0 2 0) reflection at ($2\theta = 19.1^\circ$, $d_{hkl} = 0.540$ nm) together with the increasing intensity of the composite β and γ-phase (1 1 0) reflection at ($2\theta = 23^\circ$, $d_{hkl} = 0.440$ nm). The corresponding diffraction patterns for annealed samples, Fig. 2b, show a similar decline in the proportion of α-phase crystals on application of stress and also an increase in the intensity of the γ-phase (2 1 0) reflection ($2\theta = 50^\circ$, $d_{hkl} = 0.208$ nm) which appeared as a halo in the unstressed material. The new, sharp, peak which emerges in highly stressed samples ($2\theta = 76^\circ$, $d_{hkl} = 0.145$ nm) is assigned to the (6 0 0) plane of the γ-phase. These results indicate that a partial phase transition occurs on application of a stress and this is augmented for samples annealed prior to stressing. The phase transition is not induced by the thermal annealing process. This is in contrast to the behaviour of samples annealed under stress [25].

The IR spectra, Fig. 3, confirm the XRD results with the characteristic weak bands of the α, β and γ phases appearing at 975 cm^{-1} ($t(CH_2)$), 468 cm^{-1} ($w(CF_2)$) and 950 cm^{-1} ($t(CH_2)$), respectively [26]. Although unstressed, unannealed PVDF consists mostly of the α-phase, the $t(CH_2)$ band at 950 cm^{-1} shows that a small proportion of γ-phase material is present. In

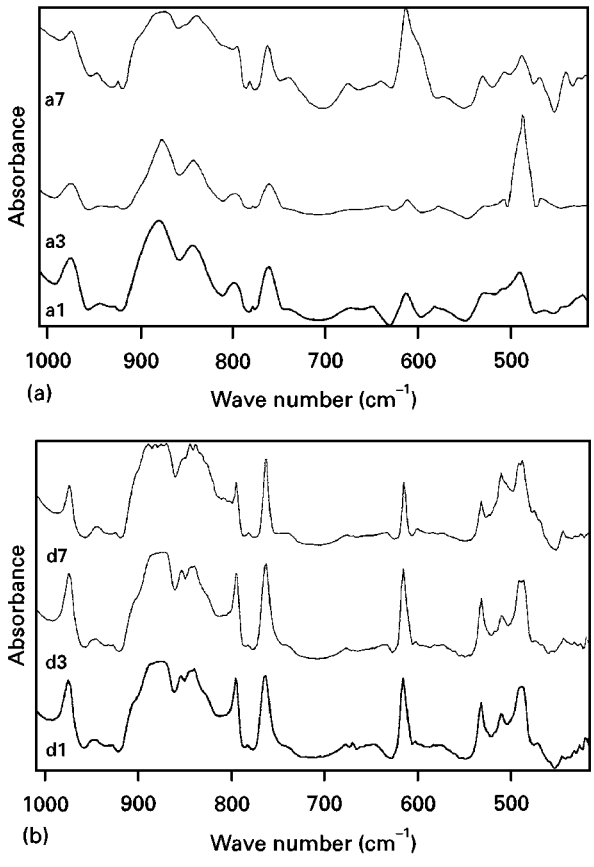

Figure 3 FT–IR absorbance spectra of (a) unannealed samples, and (b) samples annealed at 130 °C for 1 wk. Codes refer to groups of samples stressed to various stages (experimental).

the spectrum of the failed sample, the intensities of the β and γ phase bands were found to be greater than those of the corresponding bands in the unstressed material. As the tensile deformation increased, the bands in the FT–IR spectrum became narrower; this may be explained in terms of orientation effects in the direction of the applied stress [27]. Narrowing of the bands was also observed on annealing (Fig. 3b) but this is attributed to increased crystallinity.

3.2. Microscopy

Ultramicrotomed and microtomed films of unannealed and unstressed PVDF were studied by cross-polarized optical microscopy, TEM and AFM. The micrographs showed ridges running perpendicular to the stress axis (which is coincident with the extrusion axis of the pipeline). These are attributed to wavefronts produced by the flow of the polymer melt during processing [7, 23]. On annealing, the wavefront density was found to increase, apparently due to the shrinkage caused by secondary crystallization and relaxation of moulded-in-stress. On application of a tensile stress, thin voids, running parallel to the stress axis, appeared [23]. The effects of cold flow in the necked region were manifested by orientational strain-induced optical birefringence.

The effects of melting were examined. In samples which were simply allowed to resolidify, two types of spherulitic structures were identified by AFM: large spherulites corresponding to the α-phase, and smaller, coarser spherulites which were assigned to the γ-phase [12]. In accord with the FT–IR spectroscopy results for unstressed, unannealed PVDF, no β-phase spherulites could be seen in AFM images.

Samples which were melted between a glass slide and cover slip and compressed manually to produce thin films (for transmission electron microscopy studies) showed small ripples in the surface of the film, which were attributed to the folded ends of the molecules. The mean fold length was found to be 4.9 nm. By assuming that, on average, the thickness is equal to the width, the volume of a fold can be estimated. Comparison with the ***c*** vector of the unit cell of the α-phase (0.486 nm) [24] suggests that, on average, there are 20 constitutional repeat units per fold, which compares favourably with the approximate value quoted by Nakagawa and Ishida [28]. From the number of folds visible in the surface (counted over 53 nm^2), the overall fold volume per unit surface area was calculated. Similarly, by assuming a lamellar thickness of 10 nm [19], the average volume fraction of amorphous material was estimated to be 0.23.

The preferential orientation of lamellae in the plane of the sample in compressed melt-crystallized samples may be explained in terms of the inability to form long flat plates perpendicular to the compressive stress axis. The molecular segments in the bulk of such samples are parallel to the stress axis, whereas those in the surface layer are orthogonally arranged. This is manifested when the FT–IR spectra of melt-compressed and stressed-annealed samples are compared: the ν(CCC) and $r(CH_2)$ modes of the former sample are more pronounced whereas the $\nu_{as}(CH_2)$, $\nu_s(CH_2)$ and associated CF_2 stretching modes are of lower intensity. This observation is in accord with the hypothesis that in the case of melt-compressed sample the chain axis is parallel to the infrared beam.

The thermal behaviour of the group a (unannealed) samples was further investigated by DSC studies. Owing to variations in crystallite size and in accord with literature reports [28], the α-phase endotherm was seen to resolve into a peak and a shoulder in the thermograms of samples stressed to yield and beyond (samples a3–a8). At very high strain (sample a7), β and γ-phase exotherms appeared at 175 and 183 °C, respectively. These, however, were not observed in samples taken from the necked region of the failed sample (a8). The onset temperatures and enthalpies of melting, ΔH_m, and crystallisation, ΔH_c, are given in Table I. Although no obvious trend relating the onset of melting to sample number appears to be in operation, the size of the melting endotherm appears to show a general decrease with increasing stress; attributed to the drawing-induced migration of the mobile amorphous phase into the developing necked regions of the samples. The anomalous increase in ΔH_m observed with samples 5 and 6 (the onset of neck stabilization) may be explained in terms of stress-induced crystallization.

3.3. Effects of etching

3.3.1. XPS study

The effects of etching on the surface chemistry have been studied by XPS. Table II shows the spectral characteristics and elemental analyses of the surfaces of untreated and etched, melt-compressed films. On etching, the contribution of plasticizer methylene groups (C(1s)) band at 285.0 eV) to the overall XPS spectrum is reduced significantly; presumably due to the preferential distribution of the plasticizer molecules to the amorphous regions of the lamellar structure. In the etched sample, the ratio of alkyl to carbonyl carbons is 8: 1 which is consistent with the molecular formula of the plasticizer, $CH_3(CH_2)_3OOC(CH_2)_8$-$COO(CH_2)_3CH_3$. In the untreated sample, the corresponding ratio is 20 : 1, suggesting a preferential distribution of the *n*-alkane moieties of the plasticizer molecule at the surface.

TABLE I Melting and crystallization behaviour of group a samples as determined by DSC

Sample	Onset T_m (°C)	ΔH_m ($J\,g^{-1}$)	Onset T_c (°C)	ΔH_c ($J\,g^{-1}$)
1	161.3	40.9	146.3	−34.1
2	163.2	37.0	146.5	−34.0
3	159.3	34.7	147.8	−34.6
4	166.7	32.3	148.0	−32.1
5	161.4	37.6	146.7	−34.1
6	162.0	35.4	148.0	−34.9
7	162.8	29.6	148.5	−30.5
8	161.0	27.8	145.7	−33.6

TABLE II Binding energies and atomic proportions of elements at the surface of untreated and etched PVDF

	Untreated PVDF		Acid-etched PVDF		Assignments
	F_b (eV)	(at %)	F_b (eV)	(at %)	
C(1s)	285.0	25.9	285.0	15.6	Plasticizer CH_2
C(1s)	286.5	17.7	286.5	19.1	Skeletal CH_2
C(1s)	291.2	11.3	291.1	15.2	Skeletal CF_2
C(1s)	289.0	1.3	289.3	1.9	Plasticizer C = O
F(1s)	688.7	29.0	688.5	43.5	Main-chain CF_2
F(1s)	690.2	3.3	–	–	End-group CF_2
O(1s)	532.9	11.5	532.7	4.1	Plasticizer C = O

The PVDF C(1s) bands (CH_2 at 286.5 eV and CF_2 at 291.2 eV) of the XPS spectrum are assigned according to Crowe and Badyal [29]; no significant change to the relative intensities of these peaks could be observed on etching. Similarly, the covalent F(ls) band at 688.7 showed no signs of chemical modification (i.e. no significant changes in position or symmetry of peaks) as a result of the nitric acid treatment, although the relative proportion of fluorine to skeletal carbon showed a significant increase at the etched surface. This is attributed to the preferential formation of $–CHF_2$ rather than $–CH_3$ end-group functionalities following acid treatment; no evidence of the existence of sp^2 hybridized carbon residues could be identified. Following etching, the plasticiser O(1s) band at 532.9 eV decreased in intensity, thus reflecting the loss of dibutyl sebacate contained within the surface amorphous material.

3.3.2. AFM investigations

The fold surfaces in melt-compressed films were imaged by AFM [30]. In accord with expectation, the images appeared to be consistent with the switchboard model [31]. On application of the nitric acid etch, the fold patterns disappeared and the rectangular features of individual lamellae became observable.

High-resolution AFM images of etched PVDF are shown in Fig. 4a–c. The images are those of the (0 0 1) plane because the chain axes are normal to the fold surface prior to etching. To check the reproductibility of the results, images were obtained using different tips, different etched samples and by using a range of scanning parameters. The observed features were seen to increase in size proportionately when the scan range decreased, and rotation of the scan direction produced a corresponding change in the orientation of the micrographs. For example, Fig. 4b shows the orientation of a sample rotated by 45° with respect to the image in Fig. 4a. In addition, the corresponding number of atomic rows in these images is reduced by a factor of two in accord with the reduction in scan range. Forward and reverse scans supported the reproducibility of the observations. The $(1.97 \times 1.97)\,nm^2$ micrograph (shown in full in Fig. 4c) yielded an ordered Fourier pattern over the entire image and the brightest spots were selected for a transform. Application of 2d FFT removed the noise from the image without affecting the shapes and sizes of the imaged features. Although the two-dimensional unit cell can be obtained from the observed images, these are interpreted as lattice resolution which shows a convolution between tip and surface structure; in the absence of well-defined point defects or superstructures, the images cannot be described as atomically resolved.

As a further test of the validity of the observed images, density functional theory [32] (DFT) was used to simulate the relaxed positions of surface atoms in the (0 0 1) plane, from the bulk co-ordinates given by Hasegawa *et al.* [24]. The program *DSolid* [33] allows periodic systems to be investigated and a $(1 \times 1 \times 3)$ supercell was created using the known crystallographic co-ordinates. By extending the lattice vector for the supercell to 5 nm, in the ***c***-direction, the simulation was effectively performed on an array of slabs separated by a large distance, each with two (0 0 1) surfaces. A double numeric basis set with polarization functions was used, with the lattice parameters held fixed. The new atomic co-ordinates were used to generate a model of the $(1.97 \times 1.97)\,nm^2$ scanned area (Fig. 4d) and this was found to be in excellent agreement with the atomic arrangements observed by AFM.

Comparison of the AFM image (Fig. 4c) with results from the modelling study shows that only the electron-dense carbon and fluorine atoms are imaged. The periodicity of high and low rows of atoms was examined by line analysis and found to correspond very closely with the structure predicted by the model. The polymer chains are assumed to be terminated by protonated, sp^3, carbons rather than sp^2 hybridized moieties (see Section 3.3.1.)

3.3.3. Surface energy

The advancing contact angles of water, ethylene glycol and diiodomethane against the surfaces of untreated and etched melt-compressed samples of PVDF have been measured; all observations were time-independent, Table III. The contact angle of water on etched PVDF is considerably lower (8°) than for untreated samples. For diiodomethane the difference was much smaller (~2°) and there was so significant difference for ethylene glycol. Surface energy (subscript S = solid, L = liquid) components γ_S^{LW} (apolar) γ_S^+ (Lewis acid) and γ_S^- (Lewis base) have been obtained from

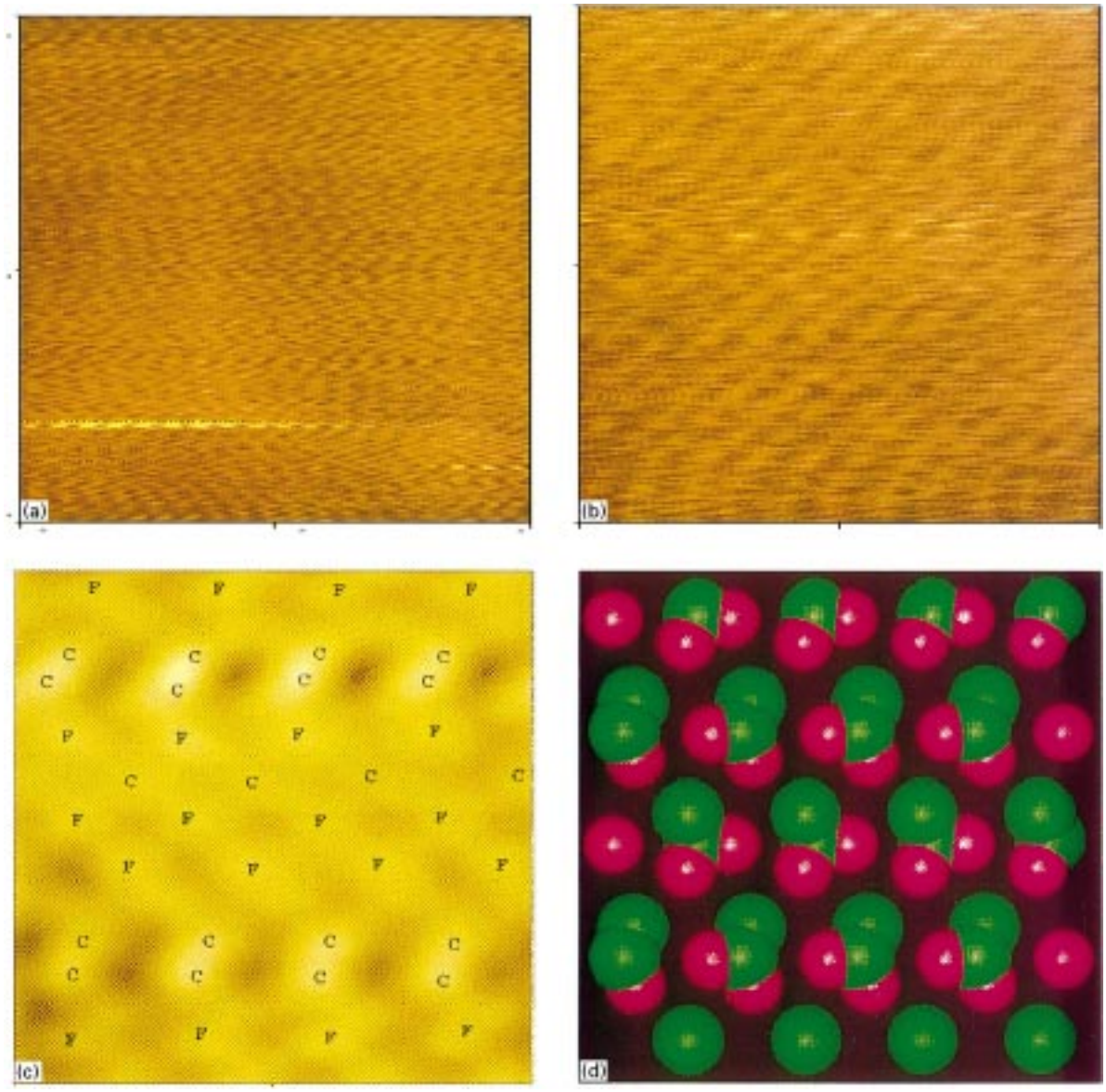

Figure 4 AFM image of the (0 0 1) surface of an etched PVDF crystal: (a) $x = y = 100$ nm (scan rate: 20 nm s^{-1}); (b) $x = y = 5$ nm (Scan rate: 20 nm s^{-1}); (c) higher resolution, Fourier transformed image from a different sample (scan rate 10 nm s^{-1}) $x = y = 1.97$ nm; and (d) relaxed (0 0 1) surface as predicted via DFT calculations; $x = y = 1.97$ nm (for clarity, hydrogen atoms are not shown).

TABLE III Contact angles of water, diiodomethane (DIM) and ethylene glycol (EG) on untreated and etched PVDF

Sample	Time(s)	Contact angle, θ (deg)			Surface energy (mJ m^{-2})			
		H_2O	DIM	EG	γ_S^{LW}	γ_S^+	γ_S^-	γ_S
Unetched	0	83.7	44.5	62.3				
	20	83.5	44.0	60.5	37.3 ± 0.3	0.02 ± 0.02	6.3 ± 0.4	38.1 ± 0.2
	40	83.6	44.5	62.5				
Etched	0	75.6	42.0	61.5				
	20	75.6	41.5	61.2	38.7 ± 0.2	0.02 ± 0.01	14.0 ± 0.5	42.3 ± 0.4
	40	75.6	42.0	62.7				

Equation 4 [34, 35]

$$\gamma_L(1 + \cos\theta) = 2[(\gamma_S^{LW}\gamma_L^{LW})^{1/2} + (\gamma_S^+\gamma_L^-)^{1/2} + (\gamma_S^-\gamma_K^+)^{1/2}] \quad (4)$$

and the surface energy of the solid, γ_S is given by

$$\gamma_S = \gamma_S^{LW} + (\gamma_S^+\gamma_S^-)^{1/2} \quad (5)$$

The surface energy of etched PVDF is higher than that of the unetched polymer by about 4 mJ m^{-2}, and this difference is associated mainly with the Lewis base contributions, γ_S. Although the results may be due to the removal of amorphous material by etching, they are also consistent with the more ordered crystalline surface (etched) having a lower entropy, if there is no difference in enthalpy between the two surfaces.

Both of the well-known models describing surface organization, the adjacent re-entry model [36] and the switchboard model [31], predict reductions in surface energy.

4. Conclusion

Annealing prior to stressing increases the yield load in plasticized PVDF as a result of secondary crystallization. Tensile deformation of the material results in a partial phase transition which is enhanced but not initiated by the annealing process. From the microscopic observations, fold surfaces in melt-grown PVDF crystals appear to form as described by the switchboard model. The folds can be removed by acid etching without altering the elemental composition of the surface layers. These etched surfaces can be imaged, at the submicrometre level, by AFM. Molecular modelling studies appear to support the interpretation of the high-resolution images.

References

1. F. SCHOLL, "Atlas of Polymer and Plastics Analysis", Vol. 3 (Hanser, Munich, 1981).
2. I. D. NEWTON, in "Polymer Characterisation", edited by B. J. Hunt and M. I. James (Blackie Academic and Professional, London 1993).
3. D. J. RUSSELL and B. MC DUFFIE, *Int. J. Environ. Anal. Chem.* **15** (1983) 165.
4. J. A. BRYDSON, "Plastics Materials", 4th Edn (Butterworth Scientific, London 1982).
5. F. MOORE, *Eng. Struct.* **11** (1989) 208.
6. F. DAWANS, J. JARRIN and J. HARDY, *SPE Prod. Eng.* **8** (1988) 387.
7. W. M. PREST Jr and D. J. LUCA, *J. Appl. Phys.* **46** (1975) 4136.
8. M. ATA, M. MACHIDA, H. WATANABE and J. SETO, *Jpn J. Appl. Phys. I Reg. Papers, Short Notes Rev. Papers* **33** (1994) 1865.
9. A. K. FRITSCHE, A. R. AREVALO, M. D. MOORE, V. B. VELINGS, K. KJOLLER and C. M. WU, *J. Membr. Sci.* **68** (1992) 65.
10. A. J. CHIPPINGDALE, R. J. PRANCE, T. D. CLARK and F. BROUERS, *J. Phys. D* **27** (1994) 2426.
11. C. LUDWIG, G. EBERLE, B. GOMPF, J. PETERSEN and W. EISENMENGER, *Annal. Physik* **2** (1993) 323.
12. A. BESSIERES, M. MEIRELES, R. CORATGER, J. BEAUVILLAIN and V. SANCHEZ, *J. Membr. Sci.* **109** (1996) 271.
13. H. HANSMA, F. MOTAMEDI, P. SMITH, P. HANSMA and J. C. WITTMAN, *Polymer* **33** (1992) 647.
14. W. STOCKER, M. SCHUMACHER, S. GRAFF, J. LANG, J. C. WITTMAN, A. J. LOVINGER and B. LOTZ, *Macromolecules* **27** (1994) 6948.
15. L. C. SAWYER and D. T. GRUBB, "Polymer Microscopy", 2nd Edn (Chapman and Hall, London, 1996).
16. F. P. REDING and E. R. WALTER, *J. Polym. Sci.* **38** (1959) 141.
17. J. RHEE and B. CRIST, *Macromolecules* **24** (1991) 5663.
18. A. KELLER, E. MARTUSCELLI, D. J. PRIEST and Y. UDAGAWA, *J. Polym. Sci. A*-2 **9** (1971) 1807.
19. P. H. GEIL, in "Polymer Single Crystals", edited by H. F. Mark and E. H. Immergut (Interscience, New York, 1963).
20. BS 2782: Part 3: "Methods 320A to 320F. Tensile Strength, Elongation and Elastic Modulus", Method 320A (BSI, London, 1976).
21. C. D. WAGNER, L. E. DAVIS, M. V. ZELLER, J. A. TAYLOR, R. H. RAYMOND and L. H. GALE, *Surf. Interface Anal.* **3** (1981) 211.
22. H.-G. ELIAS, in "Macromolecules, Structure and Properties", Vol. 1, edited by J. W. Stafford (Wiley, New York, 1977).
23. D. GLENNON, J. R. SMITH, R. T. NEVELL, D. BEGG, S. E. MASON, K. L. WATSON and J. TSIBOUKLIS, *J. Mater. Sci.*, **32** (1997) 6227.
24. R. HASEGAWA, Y. TAKAHASHI, Y. CHATANI and H. TADOKORO, *Polym. J.* **3** (1972) 600.
25. G. LAROCHE, Y. MAROIS, R. GUIDOIN, M. W. KING, L. MARTIN, T. HOW and Y. DOUVILLE, *J. Biomed. Mater. Res.* **29** (1995) 1525.
26. M. KOBAYASHI, K. TASHIRO and T. HIROYUKI, *Macromolecules* **8** (1975) 158.
27. J. N. L. KOEING, "Spectroscopy of Polymers" (Wiley Interscience, New York, 1992).
28. K. NAKAGAWA and Y. ISHIDA, *J. Polym. Sci. Polym. Phys. Ed.* **11** (1973) 2153.
29. R. CROWE and J. P. S. BADYAL, *J. Chem. Soc. Chem. Commun.* (1991) 958.
30. W. STOCKER, G. BAR, M. KUNZ, M. MOLLER, S. N. MAGONOV and H. J. CANTOW, *Polym. Bull.* **26** (1991) 215.
31. P. J. FLORY, *J. Am. Chem. Soc.* **84** (1962) 2857.
32. R. G. PARR and W. YANG, "Density Functional Theory of Atoms and Molecules" (Oxford University Press, New York, 1989).
33. *DSolid* 3.0.0 *program* (MSI, San Diego, 1995).
34. R. G. GOOD and C. J. VAN OSS, in "Modern Approaches to Wettability: Theory and Applications", edited by M. E. Schrader and G. Loeb (Plenum Press, NY 1991). pp. 1–27.
35. R. G. GOOD, M. K. CHAUDHURY and C. J. VAN OSS, in "Fundamentals of Adhesion", edited by L. H. Lee (Plenum Press, NY 1991) pp 153–172.
36. M. L. HUGGINS, *J. Polym. Sci.* **50** (1961) 65.

Received 3 November 1997
and accepted 22 April 1998